The origin of lunar crater rays

B. Ray Hawke,[a,*] D.T. Blewett,[b] P.G. Lucey,[a] G.A. Smith,[a] J.F. Bell III,[c] B.A. Campbell,[d] and M.S. Robinson[e]

[a] *Hawaii Institute of Geophysics and Planetology, School of Ocean and Earth Science and Technology, University of Hawaii, 1680 East-West Road, Honolulu, HI 96822, USA*
[b] *NovaSol, 1100 Alakea Street, 23rd Floor, Honolulu, HI 96813, USA*
[c] *Department of Astronomy, Center for Radiophysics and Space Research, Cornell University, Ithaca, NY 14853, USA*
[d] *Center for Earth and Planetary Studies, National Air and Space Museum, Smithsonian Institution, Washington, DC 20560, USA*
[e] *Center for Planetary Sciences, Northwestern University, 1847 Sheridan Road, Evanston, IL 60208, USA*

Received 26 August 2003; revised 12 February 2004

Available online 19 May 2004

Abstract

Lunar rays are filamentous, high-albedo deposits occurring radial or subradial to impact craters. The nature and origin of lunar rays have long been the subjects of major controversies. We have determined the origin of selected lunar ray segments utilizing Earth-based spectral and radar data as well as FeO, TiO_2, and optical maturity maps produced from Clementine UVVIS images. These include rays associated with Tycho, Olbers A, Lichtenberg, and the Messier crater complex. It was found that lunar rays are bright because of compositional contrast with the surrounding terrain, the presence of immature material, or some combination of the two. Mature "compositional" rays such as those exhibited by Lichtenberg crater, are due entirely to the contrast in albedo between ray material containing highlands-rich primary ejecta and the adjacent dark mare surfaces. "Immaturity" rays are bright due to the presence of fresh, high-albedo material. This fresh debris was produced by one or more of the following: (1) the emplacement of immature primary ejecta, (2) the deposition of immature local material from secondary craters, (3) the action of debris surges downrange of secondary clusters, and (4) the presence of immature interior walls of secondary impact craters. Both composition and state-of-maturity play a role in producing a third ("combination") class of lunar rays. The working distinction between the Eratosthenian and Copernican Systems is that Copernican craters still have visible rays whereas Eratosthenian-aged craters do not. Compositional rays can persist far longer than 1.1 Ga, the currently accepted age of the Copernican–Eratosthenian boundary. Hence, the mere presence of rays is not a reliable indication of crater age. The optical maturity parameter should be used to define the Copernican–Eratosthenian boundary. The time required for an immature surface to reach the optical maturity index saturation point could be defined as the Copernican Period.
© 2004 Elsevier Inc. All rights reserved.

Keywords: Moon, surface; Impact processes; Cratering; Spectroscopy; Radar

1. Introduction

Crater rays are among the most prominent lunar features. They are filamentous, high-albedo features that are radial or subradial to fresh impact craters. Rays are generally narrow in relation to the crater radius and often extend many crater radii from their parent craters. Crater rays are often discontinuous, and feathery ray elements exhibit no noticeable topographic relief. Rays from a given lunar crater often cross a variety of lunar terrains including maria, terrae, and mountain ranges (e.g., Oberbeck, 1971).

The nature and origin of lunar rays have long been the subjects of major controversies. Prior to the first spacecraft missions to the Moon, many ideas were advanced for the origin of rays. For example, Tomkins (1908) proposed a saline efflorescence hypothesis to account for lunar rays. This model involved the upward movement and evaporation of water and the deposition of salts. Nasmyth and Carpenter (1885) suggested that the lunar crust had been shattered around focal points (craters) and that lavas had been emplaced along the fractures. Among the more reasonable ideas were the suggestions that rays were (a) composed of ash

* Corresponding author. Fax: (808)-956-6322.
  E-mail address: hawke@higp.hawaii.edu (B.R. Hawke).

derived from large volcanic craters or erupted from vents associated with fractures radial to volcanic craters or (b) made of dust expelled from radial fractures produced by impact craters (see summary in Baldwin, 1949).

In the decade prior to the Apollo landings, major advances were made in lunar science. In particular, it was determined that the vast majority of lunar craters were of impact origin (e.g., Shoemaker, 1962; Schmitt et al., 1967). Earth-based telescopic images were used by Shoemaker (1962) to investigate the rays that emanate from Copernicus crater. Shoemaker (1962) interpreted rays as "thin layers of ejecta from the crater about which they are distributed." In addition, he noted the presence of elongate depressions in the Copernicus ray system and interpreted these depressions as secondary impact craters formed by individual large fragments or clusters of fragments ejected from the parent crater. Prior to Shoemaker's observations, it was generally thought that rays had no discernible topography. Baldwin (1949, 1963) stated that rays were produced by jets of rock flour that were ejected from the central crater. He suggested that rays were bright because "powdered rock is almost always whiter than the original solid."

The Ranger and Lunar Orbiter missions provided the first high-resolution images of the lunar surface. Investigations of these data by a number of workers resulted in a general agreement that rays were formed by the deposition of material from both the primary crater and secondary craters (e.g., Shoemaker, 1966; Schmitt et al., 1967; Trask and Rowan, 1967; Shoemaker et al., 1969), but neither the detailed mechanisms nor the relative significance of each component was known. Other workers emphasized the role of cometary dust from the impacting body in producing lunar crater rays (Whitaker, 1966; Mackin, 1968). Green (1971) concluded that almost all the linear and loop rays associated with Copernicus were tectonovolcanic in origin. He proposed that the craters on these rays were conjugate volcanic crater chains aligned parallel to the lunar tectonic grid in the Copernicus region. Oberbeck (1971) studied a portion of a Copernicus ray southeast of the parent crater and proposed that the bright deposits consisted of fragmental material ejected from secondary craters. Later, Oberbeck and co-workers presented a model to calculate the expected percentage of local, non-primary material within crater ejecta and ray deposits as a function of distance from the crater (Oberbeck, 1975; Oberbeck et al., 1975; Morrison and Oberbeck, 1975). Pieters et al. (1985) presented the results of a detailed remote sensing study of a portion of the ray system north of Copernicus. They provided evidence that the present brightness of the Copernicus rays in this sector is due largely to the presence of a component of highland ejecta intimately mixed with local mare basalt and that an increasing component of local material is observed in the rays at progressively greater radial distances from the parent crater. Still, the importance of secondary cratering and local mixing in producing lunar rays remains controversial. For example, Schultz and Gault (1985) have
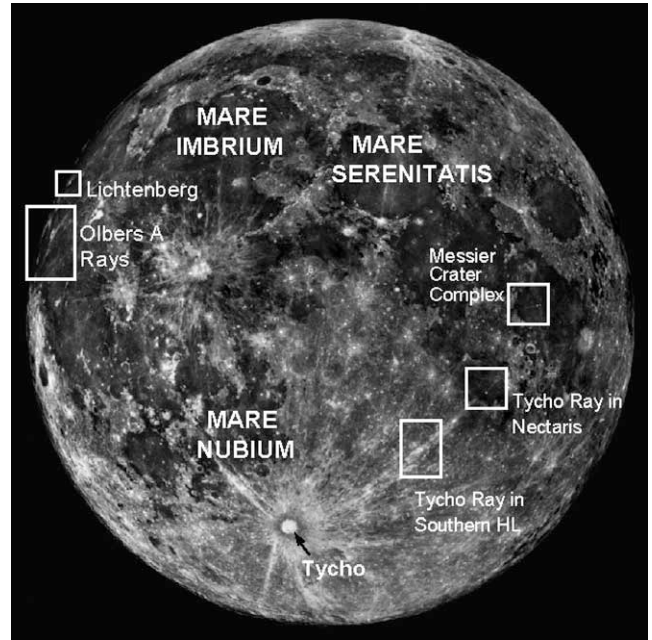

Fig. 1. Full-Moon photograph showing the locations of the crater rays investigated in this study.

presented evidence that clustered impactors are less efficient at excavating local target material than single blocks of equivalent total mass.

Fortunately, more recent spacecraft remote sensing data from Clementine allow us to better investigate the remaining problems concerning the nature of crater rays. We have used these data as well as Earth-based observations in order to further understand the processes responsible for the formation of high-albedo lunar crater rays. The purposes of this study are as follows: (1) to investigate the composition and maturity of selected lunar rays (Fig. 1), (2) to determine the origin of these rays, and (3) to assess the implications for the lunar time scale.

2. Methods

2.1. Collection and analysis of near-IR spectra

The near-infrared reflectance spectra used in this study were collected with the Planetary Geosciences InSb spectrometer mounted on the University of Hawaii 2.24-m telescope at the Mauna Kea Observatory. The instrument successively measures the intensity in 120 channels between 0.6 and 2.5 μm by rotating a filter with a continuously variable band pass in front of the detector. Circular apertures in the telescope focal plane admit light to the detector; aperture sizes of 0.7 and 2.3 arcsec were utilized. The resulting spot sizes on the surface of the Moon were $\sim$ 1.5 and 4.5 km in diameter under optimum observing conditions. The data were reduced using the techniques described by McCord et al. (1981) and Lucey et al. (1986).

Table 1
Spectral parameters derived for spectra shown in Figs. 3 and 10[1]

Spectrum ID no.	Spot name	Band min. (μm)	Contin. slope (μm^{-1})	Band depth (%)	FWHM[2] (μm)
1	Olbers A ray north	0.99	0.59	8.4	0.30
2	Olbers A ray north of Seleucus 1	0.98	0.60	12.0	0.30
3	Olbers A ray intersection 1	1.02	0.66	10.0	0.34
4	Olbers A ray intersection 2	1.00	0.66	7.9	0.31
5	Olbers A ray intersection 3	1.03	0.66	8.9	0.37
6	Crater near Olbers A ray 1	0.98	0.62	19.9	0.30
7	Crater near Olbers A ray 2	0.99	0.58	24.3	0.31
8	Olbers A ray north of Seleucus 2	0.97	0.60	12.3	0.30
9	Diffuse Olbers A ray 1	0.98	0.66	10.6	0.29
10	Diffuse Olbers A ray 2	1.01	0.65	10.2	0.32
11	Olbers A interior	0.94	0.47	5.3	0.28
12	Apollo 16	0.90	0.59	2.7	0.18
13	Mare Serenitatis 2 (MS2)	0.98	0.77	9.9	0.31
14	Messier	0.98	0.52	29.3	0.31
15	Messier ray south	0.99	0.77	19.3	0.30
16	Messier ray west	0.99	0.76	15.3	0.31
17	Messier mare west	1.01	0.74	12.1	0.34
18	Mare Nectaris ray 1	1.00	0.65	11.7	0.31
19	Ray north of Rosse	0.98	0.68	11.6	0.32
20	Mare Nectaris 2	0.98	0.67	8.5	0.30
21	Rosse	0.95	0.56	7.3	0.22

[1] The parameters are those defined by Lucey et al. (1986) and Blewett et al. (1995). The locations for which spectra obtained are shown in Figs. 2 and 9.
[2] Band full width at half maximum.

Iron-bearing mafic minerals are responsible for absorption bands in lunar spectra near 1 μm. The shape and position of this band provide information concerning the composition and relative abundance of pyroxene and olivine (e.g., Adams, 1974). In order to extract this information, a number of spectral parameters were determined using the methods described by Lucey et al. (1986) and Blewett et al. (1995). The spectral parameters for the near-IR spectra used in this study are listed in Table 1.

Both maturity and composition control the near-IR continuum slope (Δ reflectance/$\Delta\lambda$), with higher Fe and more-mature surfaces exhibiting spectra with steeper continuum slopes. The near-IR continuum slope is measured by fitting a straight line tangent to points on the spectrum on either side of the "1 μm" band, typically near 0.7 and 1.6 μm.

In order to gain further insight into the spectral data set, the multivariate statistical technique of principal components analysis (PCA) was applied to selected near-IR spectra. A method of using PCA for spectral data was developed by Smith et al. (1985) and applied to lunar telescopic and sample spectra by several workers (e.g., Johnson et al., 1985; Pieters et al., 1985; Blewett et al., 1995; Blewett and Hawke, 2001). PCA reduces the dimensionality of the data to a small number of factors (components) related to the causes of the variation, aiding in the selection of spectral endmembers and revealing mixing trends. We conducted PCA for Olbers A ray-related spectra using the methods described by Blewett et al. (1995) and Blewett and Hawke (2001). For reference, spectra for the Apollo 16 site and the Mare Serenitatis (MS2) spectral standard site were also included in the PCA.

The PCA was performed on spectra relative to the Sun, scaled to 1.0 at 1.02 μm. In order to prepare the spectra for PCA, the portions of the spectra susceptible to thermal contamination (longward of 2 μm) and in the vicinity of telluric water absorptions (near 1.4 and 1.9 μm) were deleted. The spectra were thus defined by reflectances at 69 wavelengths between 0.67 and 1.81 μm.

The variance–covariance matrix of the spectral data matrix was calculated, and the eigenvectors and eigenvalues extracted. It was determined that the first two principal components are responsible for over 95% of the variation in the data. The relationship of the principal components to physically meaningful quantities was examined by plotting the eigenvectors against wavelength. It was determined that the first principal component is mainly related to the characteristics of the mafic mineral absorption band near 1 μm. The second principal component is sensitive to the spectral slope. Principal component scores for the near-IR spectra were calculated by transforming each spectrum by the eigenvectors. Each spectrum may then be located as a single point in PC space (Fig. 11). When plotted in this manner, potential endmembers fall at the extremes, and mixtures lie within the area demarcated by the endmembers (Smith et al., 1985). The distance of a mixture from a plausible endmember provides a measure of the relative contribution of that endmember to the mixture. Three-component mixing studies were conducted using mature mare (MM, spectrum 13, MS2), fresh mare (FM, spectrum 7, Crater near Olbers A ray 2) and average highlands (HL) as endmembers. The HL endmember was created by averaging the Apollo 16 (spectrum 12) and the Olbers A interior

Table 2
Spectral mixing model results based on PCA for Olbers A ray spectra

Spectrum ID	Spot name	Average highlands (%)[a]	Mature mare (%)[a]	Fresh mare (%)[a]
1	Olbers A ray north	60	21	19
2	Olbers A ray N of Seleucus 1	42	17	41
8	Olbers A ray N of Seleucus 2	39	23	38
3	Olbers A ray intersection 1	32	53	15
4	Olbers A ray intersection 2	45	49	6
5	Olbers A ray intersection 3	42	51	7
9	Diffuse Olbers A ray 1	29	51	20
10	Diffuse Olbers A ray 2	35	50	15

[a] % of flux contributed to each spectrum.
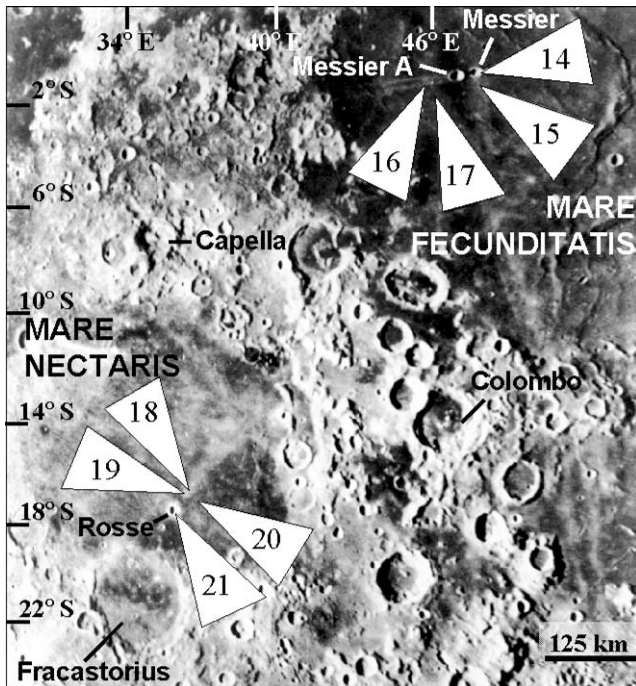
Fig. 2. Rectified Earth-based telescopic photograph of Mare Nectaris and a portion of Mare Fecunditatis (part of Plate 20-d of Whitaker et al. (1963)). The numbered arrows indicate the locations for which near-IR reflectance spectra were obtained for the Messier crater complex and the Tycho ray in Mare Nectaris. The numbers correspond to those of the spectra shown in Fig. 3 and listed in Table 1.

(spectrum 11) spectra. The resulting submature highlands endmember is labeled "11.5" in Fig. 11. The results of the three-component mixing model study are presented in Table 2.

2.2. Clementine UVVIS images

In order to gain spatial information on the composition and maturity of units in the various ray regions, Clementine UVVIS images were utilized. Maps of FeO and TiO_2 abundances with a resolution of ~ 100 m/pixel were prepared for each ray region. The techniques developed by Lucey and co-workers (Lucey et al. 1995, 1998, 2000a; Blewett et al., 1997) were applied to calibrated Clementine images in order to produce the FeO and TiO_2 maps. In addition, optical ma-

turity (OMAT) images were produced for each ray using the spectral algorithms presented by Lucey et al. (2000b). Optical maturity parameter data are useful for investigating the relative ages of deposits associated with lunar rays.

2.3. Radar data

The radar data, at wavelengths of 3.0, 3.8, and 70 cm, were used to describe the surface and near-surface roughness of the rays, and thus to assess the degree to which fragmental debris characterizes ray surfaces and secondary crater ejecta. The polarized and depolarized 3.0-cm radar data used in this study exists only for the Tycho ray in Mare Nectaris. This data was first presented in Fig. 15 of Campbell et al. (1992) and information concerning the collection and processing of the images is provided in that paper. The spatial resolution of the 3.0-cm radar images is ~ 60 m.

The 3.8-cm radar data utilized in this investigation were those obtained by Zisk et al. (1974). The 3.0-cm and 3.8-cm maps were compared to 70-cm wavelength radar images produced by Thompson (1987). These 70-cm images have a spatial resolution of ~ 3 km and were collected in both senses of received circular polarization. The 70-cm data complement the 3.0- and 3.8-cm images in that they are sensitive to roughness on spatial scales from 50 cm to 10 m and penetrate 5–10 m into the regolith. In contrast, the 3.0- and 3.8-cm radar signals were typically sensitive to roughness on scales of 1–50 cm within the upper meter of the regolith.

3. Results and discussion

3.1. Messier crater complex

The Messier crater complex is located near 2° S, 47° E in Mare Fecunditatis on the nearside of the Moon (Figs. 1 and 2). The complex consists of Messier crater (14 km in long dimension) and Messier A crater (diameter = 11 km) and their associated ejecta and ray deposits (Figs. 2 and 4a). Major rays extend north and south from Messier and west from Messier A. A well-developed ray excluded zone occurs east of Messier. A variety of factors suggest that Messier and Messier A were formed by the oblique impact of one or more
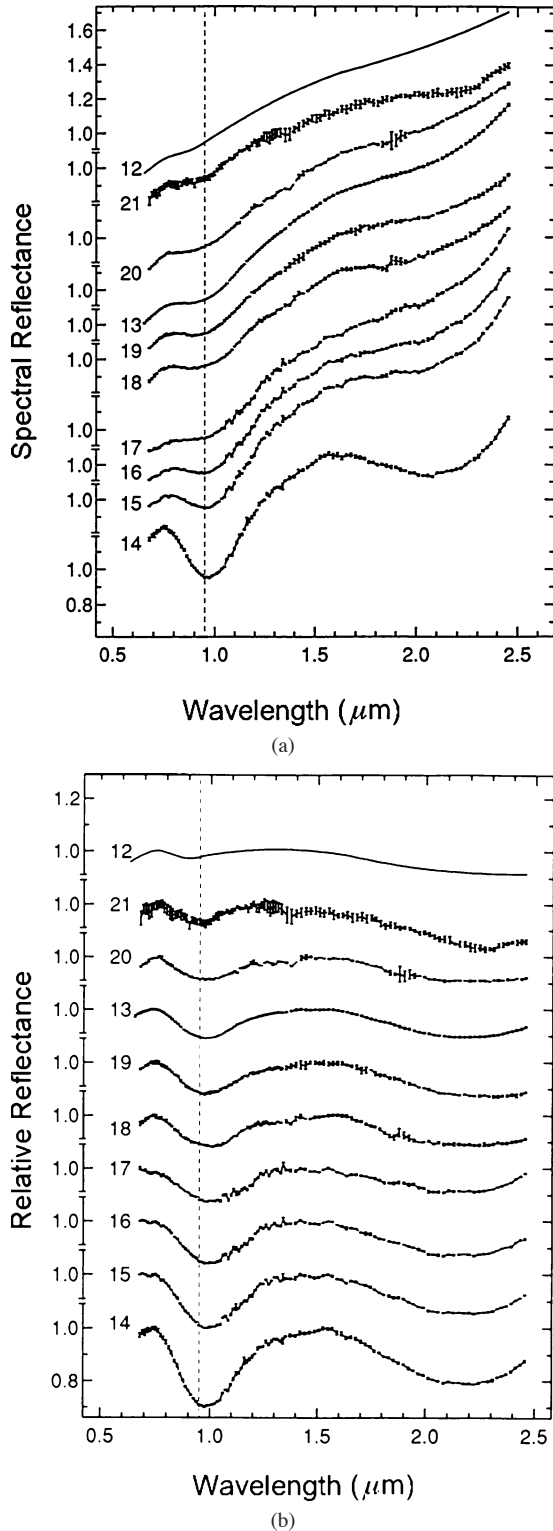
(a)

(b)

Fig. 3. (a) Near-IR reflectance spectra for the locations given in Fig. 2 and listed in Table 1. The spectra have been offset for clarity and are scaled to 1.0 at 1.02 μm. The vertical dashed line is located at 0.95 μm. (b) Continuum-removed versions of the spectra shown in (a).

and (3) the elongate shape of Messier crater. Schultz (1976) noted that Messier A was a complex feature and suggested that it could be the result of an oblique impact partially overlapping an older crater. Apollo orbital X-ray fluorescence data were used by Andre et al. (1979) to demonstrate that Messier A excavated magnesium-rich mare basalt from beneath less-magnesian surface units in Mare Fecunditatis.

Near-IR spectra were obtained for portions of the rays west and south of the crater complex, as well as for Messier and nearby mature mare surfaces. The areas for which spectra were collected are indicated in Fig. 2 and the spectra are shown in Figs. 3a and 3b. The spectral parameters derived for these spectra are listed in Table 1. The spectrum obtained for the interior of Messier crater (no. 14) exhibits an extremely deep (29%) ferrous iron absorption band centered at 0.98 μm. The mafic assemblage is dominated by high-Ca pyroxene; a fresh mare composition is indicated. In addition, Messier and Messier A exhibit strong returns on both the 3.8- and 70-cm depolarized radar images. The interiors of these craters are enriched in blocks (0.5–10 m) and smaller rock fragments (1–50 cm).

Spectra were collected for portions of the rays west and south of the Messier crater complex (Figs. 2 and 3). The spectrum collected for the ray west of Messier A (no. 16) has a 15% absorption feature centered at 0.99 μm. The mature mare unit adjacent to this ray has a spectrum (no. 17) that exhibits a shallower absorption band with a similar band center. The FeO image (Fig. 4b) shows that the west ray exhibits FeO values (16–17 wt%) slightly less than those of adjacent mare deposits (17–18 wt%). The TiO$_2$ values (3.0–4.0 wt%) exhibited by the west ray are lower than those of the nearby mare units (4.0–6.0 wt%) but are similar to those exhibited by portions of the proximal ejecta deposits of Messier and Messier A (Fig. 4c). The above evidence indicates that the ray west of Messier A is dominated by relatively immature mare basalt. However, the FeO and TiO$_2$ values obtained for this ray indicate that the basaltic material in the west ray has a composition different from those of adjacent mare units.

Additional evidence for the immaturity of the west ray is provided by the radar and optical maturity images. The west ray has slightly enhanced values in the depolarized 3.8-cm radar image, but no enhancement is apparent in the 70-cm data set. Hence, the upper portion of the ray is enriched in fragments in the 1–50 cm size range, but is not enriched in blocks (0.5–10 m). The optical maturity image (Fig. 4d) shows that the west ray is relatively immature. The ray exhibits typical OMAT values of 0.18 to 0.20. Nearby mare surfaces have lower OMAT values of 0.13–0.14, consistent with a mature background.

One near-IR spectrum was obtained for a portion of a ray south of Messier crater (no. 15 in Figs. 2 and 3). This spectrum exhibits a deep (19%) absorption band with a minimum at 0.99 μm (Table 1) indicating that the area for which it was collected is dominated by mare basalt. The FeO values (17–18%) and TiO$_2$ values (4–6%) exhibited by the ray south of Messier are similar to those determined for adjacent mare

projectiles that approached from the east. The evidence for low-angle impact includes (1) the asymmetrical distribution of ejecta and rays, (2) the presence of a ray excluded zone,
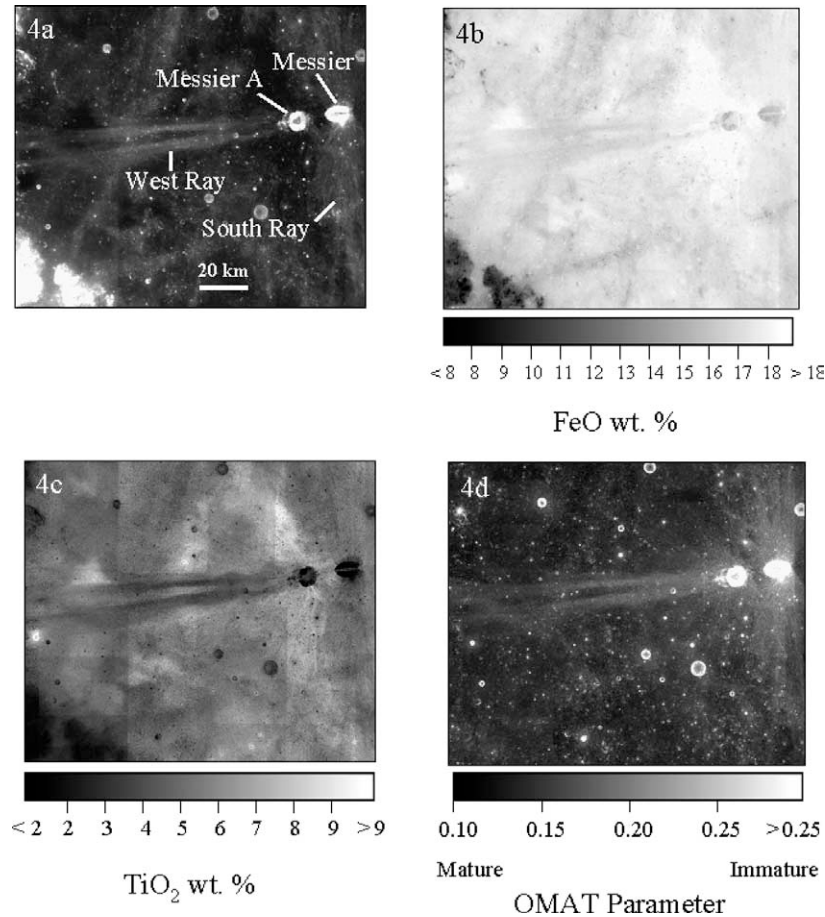
Fig. 4. (a) Clementine 750 nm image showing the Messier crater complex under high Sun illumination. North is to the top. (b) FeO map derived from Clementine UVVIS images. This map is for the same area as the 750 nm image shown in (a). (c) TiO$_2$ map produced from Clementine UVVIS images. The map is for the same area as the 750 nm image shown in (a). (d) Optical maturity parameter image produced for the Messier crater complex. Brighter tones indicate lower maturity (fresher material). Note that the rays associated with the Messier crater complex are relatively immature.

surfaces (Figs. 4b and 4c). The optical maturity parameter image (Fig. 4d) shows that the south ray is relatively immature.

In summary, the rays west and south of the Messier complex are prime examples of "immaturity" rays. They are composed of immature mare material. These rays are bright because they contain immature basaltic debris. Highlands material is not present in the rays. Compositional differences play little, if any, role in producing the albedo contrast exhibited by the south ray. However, since the basalts in the west ray are lower in TiO$_2$ than the adjacent mare deposits, compositional differences may make a minor contribution to the albedo contrast of this ray, since basalts higher in TiO$_2$ are generally darker.

3.2. Tycho ray in Mare Nectaris

A major ray from Tycho crater crosses much of Mare Nectaris (Figs. 1 and 2). The 80-km long segment of this Tycho ray northeast of Rosse crater (17.9° S, 35° E) has a somewhat conical shape, ranging in width from 8 km near Rosse to 16 km northwest of Bohnenberger crater. Here, we

have focused our attention on that portion of the ray that extends ∼ 40 km northeast of Rosse (diameter = 12 km) and includes a Tycho secondary crater cluster (Figs. 5 and 6a). Further to the northeast, the structure and composition of this Tycho ray is difficult to determine because of the presence of Theophilus rays in this area.

Near-IR spectra were obtained for Rosse crater, mature mare, and two small areas on the Tycho ray northeast of Rosse (Figs. 2 and 3). Both of the ray spectra (no. 18, 19) were collected for areas located near a Tycho secondary crater cluster which is ∼ 1400 km from the center of the parent crater. The spectrum collected for Rosse crater (no. 21) has a 7% absorption feature with a band minimum at 0.95 μm (Table 1). The spectral parameters derived for this spectrum suggest that Rosse penetrated through the Nectaris mare and excavated both mare and highlands material. Rosse is surrounded by a halo of material which exhibits FeO values of 10–12% (Fig. 6b) further suggesting an admixture of highlands and mare debris.

The spectral parameters derived for the other spectra collected in the vicinity indicate a mare composition. The spectrum obtained for a mature mare area east of Rosse (no. 20,
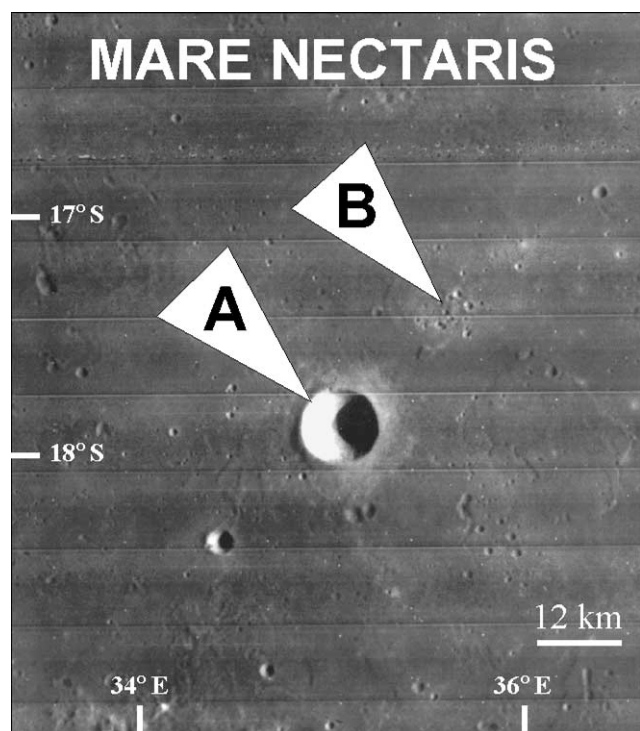
Fig. 5. Lunar Orbiter photograph (LO IV-72-H2) of a portion of Mare Nectaris. Arrow A indicates Rosse crater and arrow B indicates a Tycho secondary crater cluster.

Mare Nectaris 2 in Table 1) exhibits an 8.5% absorption feature centered at 0.98 μm. Both ray spectra (no. 18, 19) have $\sim$ 12% bands centered at $\sim$ 0.99 μm. It appears that the Tycho ray is dominated by relatively fresh mare debris in the areas for which the spectra were collected, despite the fact that the Tycho ejecta itself is composed of highlands material.

Campbell et al. (1992) noted that Rosse crater was only just visible in the 70-cm images and that the nearby ray segment exhibited no trace of associated roughness on meter scales. The Tycho secondaries in the cluster (Fig. 5) are easily seen in the 3.0-cm radar images, and a radar-bright area extends 10–15 km downrange of Tycho from the center of the cluster. Campbell et al. (1992) noted that the radar-bright region exhibited a deeper "1 μm" feature as evidenced by multispectral ratio images and suggested that fragmental material was emplaced well downrange of the visible secondaries, perhaps by a secondary debris surge.

The FeO and optical maturity images (Figs. 6b and 6d) provide additional information that supports the above interpretation. The OMAT image demonstrates that the craters in the cluster are immature. The radar-bright area that extends downrange from the secondary cluster is also relatively immature. In order to influence the optical maturity image, at least some of the small fragments detected by the 3.0-cm radar images must be exposed at the very surface of the ray. The FeO image shows that the FeO values exhibited by the secondary cluster and its downrange deposits are very similar to those of adjacent mature mare surfaces (14–16 wt% FeO). Some highlands debris derived from the

Tycho secondary-forming projectiles must be present in this segment of the ray. Perhaps the portions of the ray that exhibit slightly lower FeO values (Fig. 6b) contain more Tycho primary ejecta. This small highland component is completely dominated by local mare basalt excavated during the secondary-forming events. These finding are in general agreement with the local mixing hypothesis described by Oberbeck (1975).

In summary, the southwestern portion of the Tycho ray in Mare Nectaris (Figs. 5 and 6) is an example of an "immaturity" ray. It is composed largely of immature mare basalt with little to no detectable Tycho ejecta material. The brightest portion of this ray segment is produced by the immature interiors of the craters in the Tycho secondary cluster. Fresh material is constantly being exposed on these crater walls due to downslope movement. The high-albedo material immediately downrange of the cluster is dominated by relatively immature mare debris. Some highland material derived from the Tycho secondary-forming projectiles must be present. This nonmare material makes a very minor contribution to the brightness of this ray segment because of its composition and immaturity. Finally, it should be noted that these results are only for the Tycho ray element shown in Figs. 5 and 6. Other portions of the Tycho ray in Mare Nectaris are very complex and some parts appear to contain a significant highlands component.

3.3. Tycho ray in southern highlands

We have also investigated another segment of the Tycho ray discussed above in the highlands southwest of Mare Nectaris (Fig. 1). The ray segment studied extends from just southwest of Wilkens crater (30° S, 19° E) to the Rupes Altai, a major ring of the Nectaris basin. The 750 nm image of this ray is shown in Fig. 7a. The FeO image (Fig. 7b) shows that the ray has the same range of FeO values (5.5–7.0 wt%) as that exhibited by the adjacent highlands terrain. There appears to be no difference in composition between the ray and the nearby highlands. Hence, compositional differences played no measurable role in the formation of this portion of the Tycho ray.

The optical maturity parameter image (Fig. 7c) demonstrates that the high-albedo portions of this ray segment are composed of immature material. The highest albedo, most immature areas seen in Figs. 7a and 7c are associated with Tycho secondary crater chains and clusters (black arrows in Figs. 7a and 7c). The areas immediately downrange from these secondary crater chains and clusters are also relatively immature. Tycho secondary-forming projectiles excavated fresh, local highlands material. Immature Tycho primary ejecta mixed with immature, local debris during the cratering process, and the resulting secondary ejecta was emplaced largely downrange of Tycho. Lucchitta (1977) has described debris flows that are often formed downrange of major Tycho crater clusters by the emplacement of low-angle sec-
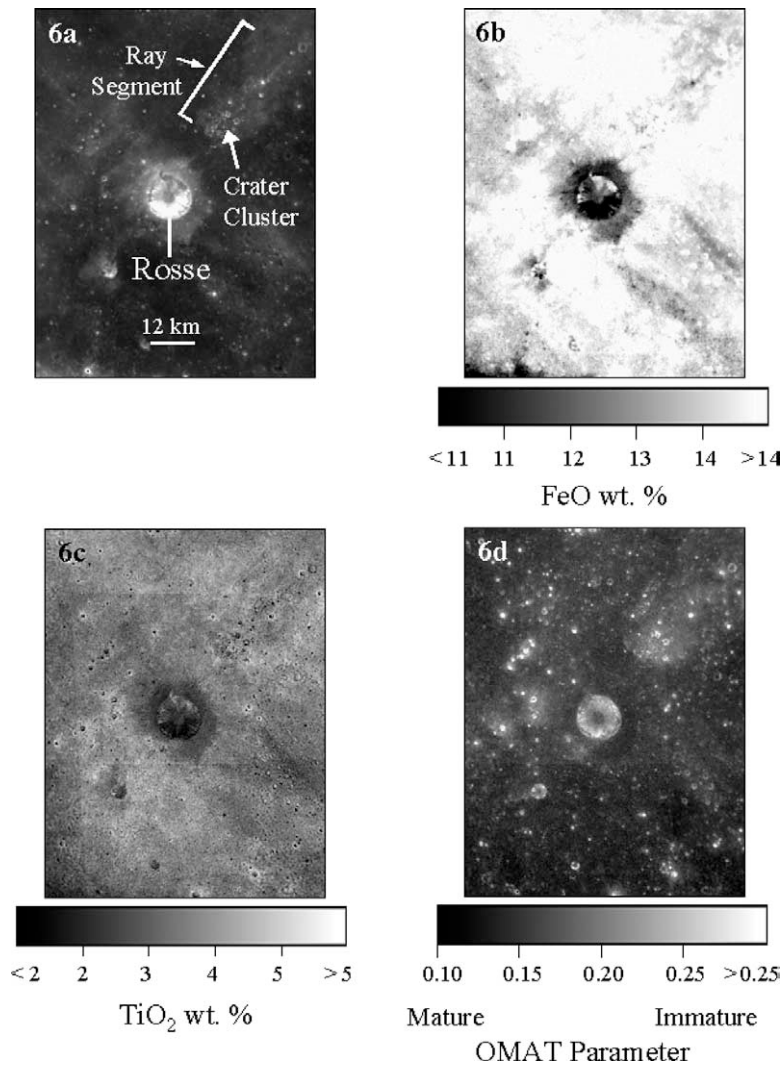
Fig. 6. (a) Clementine 750 nm image of a Tycho ray segment in Mare Nectaris. North is to the top. (b) FeO map derived from Clementine UVVIS images. The map is for the area shown in (a). (c) TiO$_2$ map derived from Clementine UVVIS images. The map is for the area shown in (a). (d) Optical maturity parameter image produced for the Tycho ray segment in Mare Nectaris. Note that the Tycho secondary crater clusters and the associated ray segment are relatively immature.

ondary ejecta. Such secondary debris surges would cover and/or disrupt preexisting mature surfaces.

This portion of the Tycho ray is composed of relatively fresh highland debris. Since highland projectile material from Tycho was mixed with local highland material, it is not possible with currently available spectral or compositional data to assess the relative importance of local mixing in producing the Tycho ray in the southern portion of the central highlands. However, the high albedo of this ray is totally due to the immaturity of the highland debris.

3.4. Lichtenberg crater rays

Lichtenberg crater (diameter = 20 km) is located in Oceanus Procellarum on the northwestern portion of the lunar nearside (31.8° N, 67.7° W). This impact structure displays a relatively high-albedo ejecta blanket and ray system to the north and northwest (Figs. 1 and 8a). Us-

ing the criteria first set forth by Shoemaker and Hackman (1962), Lichtenberg has been mapped as a Copernican-aged impact crater by several workers (e.g., Moore, 1967; Wilhelms, 1987). Lichtenberg ejecta is embayed by mare basalt south and southeast of the crater (Schultz, 1976; Allen, 1977; Schultz and Spudis, 1983). Because of this embayment relationship, this mare deposit has also been considered to be of Copernican age and among the youngest basalt flows on the Moon.

The FeO map produced for the Lichtenberg region (Fig. 8b) indicates that the ejecta and rays north and northwest of the crater exhibit lower FeO abundances (11–14 wt%) than nearby mare surfaces (> 16 wt%). The FeO values associated with Lichtenberg ejecta are within the range of values exhibited by exposures of highland rocks in this portion of the lunar nearside (Lucey et al., 2000a). The lowest FeO values are associated with the continuous ejecta deposits of Lichtenberg as well as the brighter por-
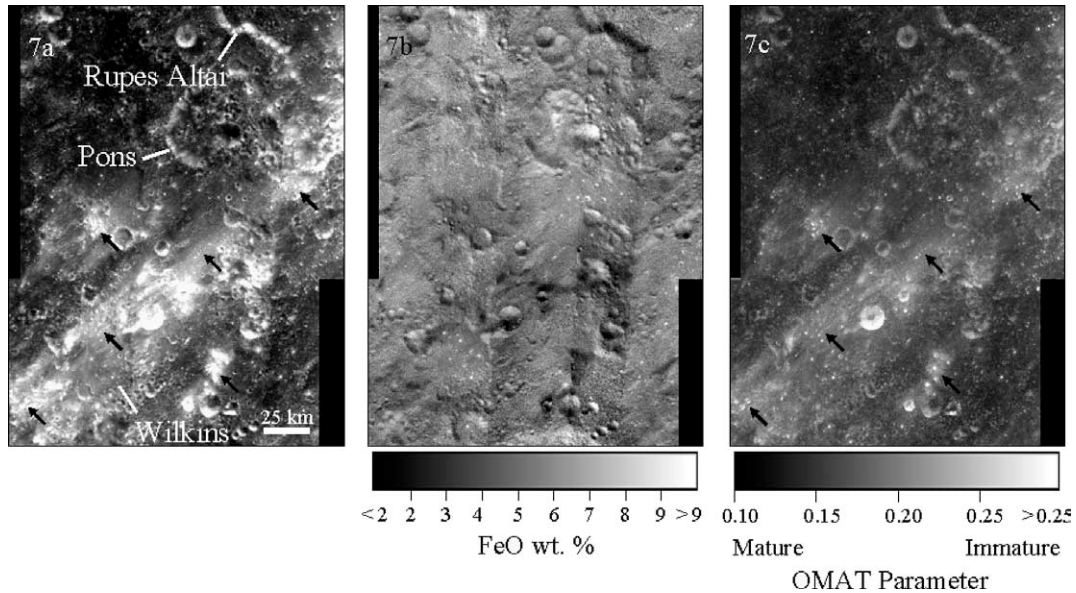
Fig. 7. (a) Clementine 750 nm image mosaic showing a Tycho ray segment in the southern highlands. The black arrows indicate Tycho secondary crater chains and clusters. North is to the top. (b) FeO map for the area shown in (a). The Tycho ray has the same range of FeO values as that exhibited by the adjacent highlands terrain. (c) Optical maturity parameter image for the area shown in (a). The black arrows indicate Tycho secondary crater chains and clusters. These crater chains and clusters and the areas immediately downrange are relatively immature.

tions of the rays. Slightly higher FeO values are exhibited by the discontinuous ejecta deposits and the more diffuse ray segments (Fig. 8b). A small dark-haloed impact crater (Fig. 8a) has excavated FeO-rich mare basalt from beneath the highland-rich Lichtenberg ejecta blanket. The FeO data indicate that Lichtenberg ejecta and ray deposits contain abundant highland debris. The TiO_2 map (Fig. 8c) supports this interpretation. The mare units that surround Lichtenberg exhibit TiO_2 abundances that range from 3 to 11 wt%. Lower TiO_2 values (1–3 wt%) are associated with the Lichtenberg ejecta and rays. It is not surprising that Lichtenberg excavated highland material from beneath the mare basalt flows. The mare deposits are fairly thin in this portion of Oceanus Procellarum (De Hon, 1979). Lichtenberg is superposed on the rim of a flooded pre-mare crater. Portions of the rim of this flooded crater extend above the surrounding mare surface (black arrows in Fig. 8a). Hence, some highland material was probably present at or near the surface in the Lichtenberg pre-impact target site.

An optical maturity parameter image of the Lichtenberg region is shown in Fig. 8d. The Lichtenberg ejecta blanket exhibits OMAT values of 0.14–0.15. Similar values are exhibited by mature mare surfaces in the region, thus the ejecta deposits of Lichtenberg crater are fully mature (e.g., Hawke et al., 1999; Grier and McEwen, 2001). The presence of immature debris plays little or no role in producing the brightness of the Lichtenberg rays. These rays are visible only because of compositional differences between the mature highlands-rich ray material and the adjacent mature mare surfaces (Hawke et al., 1999, 2000). The Lichtenberg rays are prime examples of "compositional" rays.

These "compositional" rays stand in stark contrast to the "immaturity" rays such as those associated with the Messier crater complex. With increasing age, the Messier rays and the Tycho ray segments discussed above will become more mature. Eventually, their surfaces will reach full optical maturity and they will not be visible. Compositional rays such as those associated with Lichtenberg crater will not disappear when the ray surfaces become fully mature. These rays will become indistinct only when the highland material in the rays has been fully diluted by mare debris introduced by vertical mixing or lateral transport from adjacent mare units. It should be noted that the mixing and dilution process takes much longer than the maturation process (e.g., Pieters et al., 1985; Blewett and Hawke, 2001).

As discussed above, Lichtenberg has been mapped as a Copernican-aged crater (e.g., Wilhelms, 1987). The ejecta deposits of Lichtenberg crater are embayed by mare basalt flows that have recently been estimated to have an age of $1.68^{+0.30}_{-0.12}$ Ga (Hiesinger et al., 2003). These basalt flows cover a much older mare unit ($3.18^{+0.08}_{-0.10}$ Ga) which may also embay Lichtenberg ejecta (Hiesinger et al., 2003). Hence, Lichtenberg crater is older than 1.68 Ga, perhaps much older. Lichtenberg is also older than Copernicus, which has been dated at ~ 0.80 Ga (Eberhardt et al., 1973; Bogard et al., 1994; Stöffler and Ryder, 2001). Lichtenberg has an age greater than the commonly accepted date (1.1 Ga) for the Copernican–Eratosthenian boundary (e.g., Wilhelms, 1987). It is now clear that Lichtenberg is not a Copernican-aged crater. Other craters that exhibit compositional rays may be older than the Copernican–Eratosthenian boundary. The mere presence of rays is not a reliable indicator of crater age.
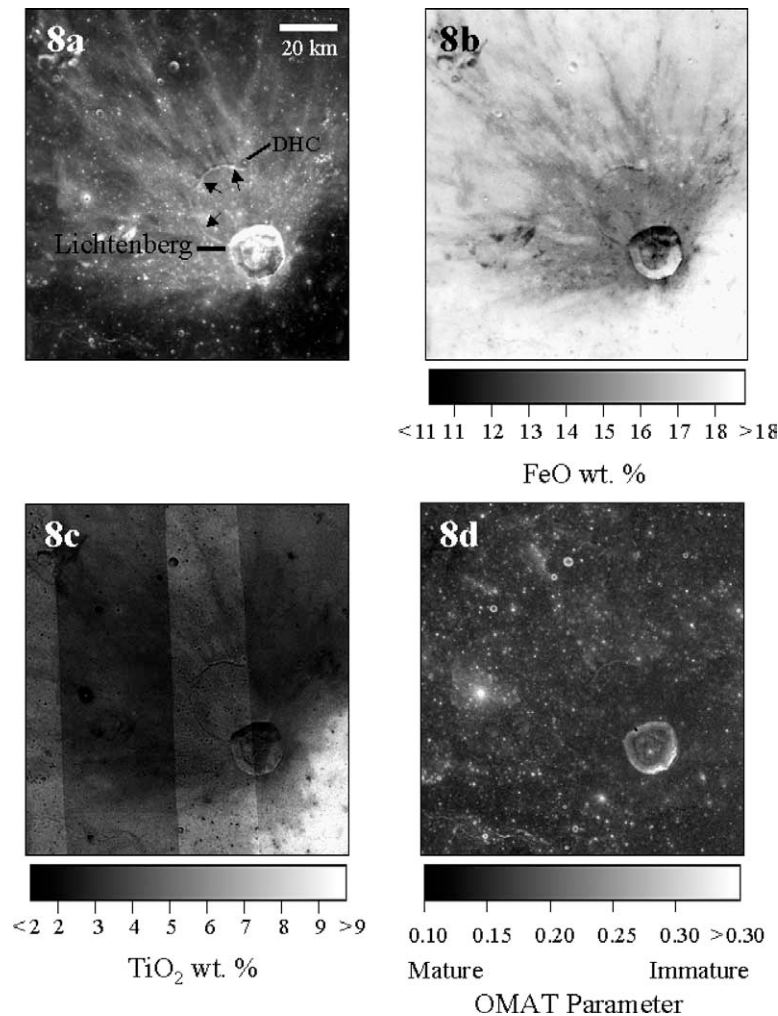
Fig. 8. (a) Clementine 750 nm image of the Lichtenberg crater region. The black arrows indicate portions of the rim of a flooded crater that extend above the surrounding mare surface. DHC indicates a dark haloed impact crater that has excavated FeO-rich mare basalt from beneath the highland-rich Lichtenberg ejecta blanket. North is to the top. (b) FeO map of the Lichtenberg crater region. (c) TiO$_2$ map of the Lichtenberg crater region. (d) Optical maturity parameter image of the Lichtenberg crater region. Note that the Lichtenberg ejecta blanket is optically mature.

3.5. Olbers A ray system

Olbers A, a 43-km diameter impact crater located in the highlands on the Moon's western limb (8.1° N, 77.6° W), exhibits an extensive ray system (Fig. 1). Olbers A has been mapped as a Copernican-aged crater (e.g., Wilhelms, 1987). Eight near-IR reflectance spectra were obtained for prominent rays that extend northeast from Olbers A across Oceanus Procellarum (Fig. 9). Three of these spectra are for small (3–6 km in diameter) areas near the intersection of two major ray elements approximately 385 km northeast of Olbers A. Three spectra were collected for a portion of the ray immediately northeast of Seleucus crater (Fig. 9). This ray segment is approximately 550 km from the rim of the parent crater. Two spectra were obtained for diffuse ray elements in the same general area. Spectra were also obtained for the interior of Olbers A crater as well as fresh mare craters near the ray. These spectra are shown in Fig. 10.

An analysis focusing on the mafic mineral absorption band near 1 μm was performed on all spectra, the results of which are given in Table 1. Spectral mixing model studies based on the results of principal components analysis (PCA) were also conducted using the techniques described by Blewett et al. (1995). A plot of the principal component scores of Olbers A ray-related spectra is given in Fig. 11 and the results of the spectral mixing model study are presented in Table 2.

The spectral parameters determined for three spectra (no. 3, 4, and 5) collected for areas near the intersection of ray elements south of Seleucus (Fig. 9) indicate that these areas are dominated by mare material. All exhibit mafic absorption bands centered longward of 0.95 μm indicating the presence of high-Ca pyroxene. However, the spectra for the ray intersection (no. 3, 4, and 5) lie along a mixing line between mature mare (no. 13) and average highlands (no. 11.5) on the PC space plot of Fig. 11. The spectral mixing model results (Table 2) suggest that highland debris contributes 32
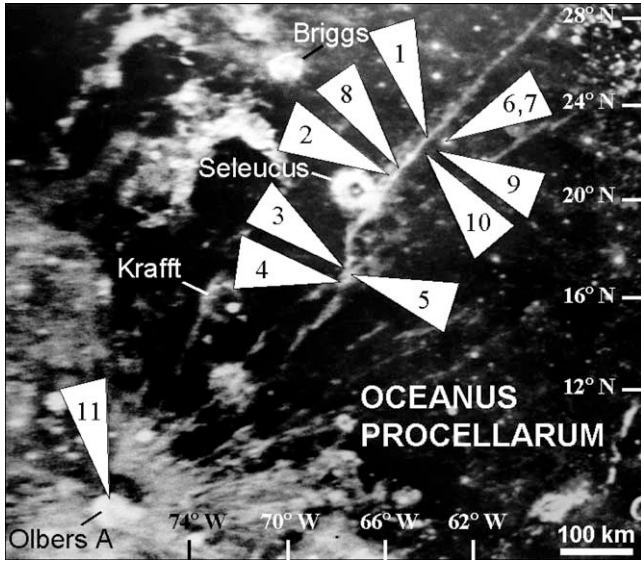
Fig. 9. Rectified Earth-based telescopic photograph showing the Olbers A ray system in Oceanus Procellarum (part of Plate 10-c of Whitaker et al. (1963)). The numbered arrows indicate the locations for which near-IR reflectance spectra were obtained. The numbers correspond to those of the spectra shown in Fig. 10 and listed in Table 1.

to 45% of the flux to the spectra obtained near the ray intersection. While mare material dominates the areas for which the spectra were obtained, fresh mare material contributes only 6 to 15% of the flux to these spectra. The evidence suggests that significant amounts of Olbers A primary highland ejecta is present in the vicinity of the ray intersection.

The FeO and TiO_2 maps (Figs. 12b and 12c) provide additional evidence for the presence of nonmare debris near the ray intersection. In the area for which the spectra were collected, FeO values range from 13 to 16 wt% and TiO_2 values range from 3 to 5 wt%. The adjacent mare surfaces exhibit FeO abundances greater than 16 wt% and have TiO_2 abundances of 6 to 8 wt%. It is important to note that the area of the ray intersection is not distinct in the optical maturity image (Fig. 12d). Immature material is present only on the interiors of a small number of craters. This observation suggests that the presence of immature material plays only a minor role in producing the high albedo of the Olbers A rays near the intersection.

Three near-IR spectra (no. 1, 2, and 8) were obtained for an Olbers A ray northeast of Seleucus crater, and two spectra (no. 9 and 10) were collected for a more diffuse portion of the same ray (Fig. 9). Three of these spectra (no. 1, 9, and 10) lie close to a mixing line between the mature mare and average highland endmembers on the PC space plot (Fig. 11). Two spectra (no. 2 and 8) are offset toward the fresh mare endmember. An examination of the original observing photographs, taken when the spectra were obtained to document the exact location of the aperture on the lunar surface, revealed that these two spectra (no. 2 and 8), which were collected with larger apertures, contain flux from the bright interiors of mare craters that are unrelated to the ray. Hence, these spectra will be excluded from further discussion.
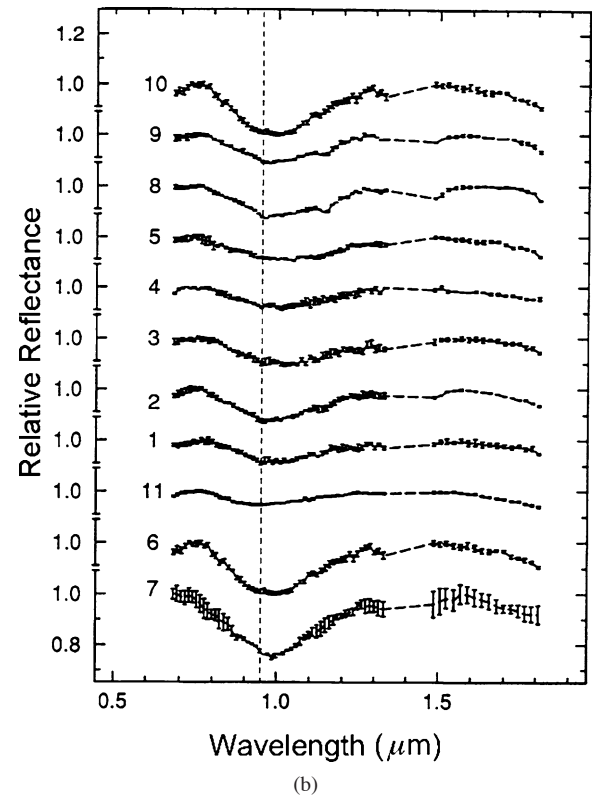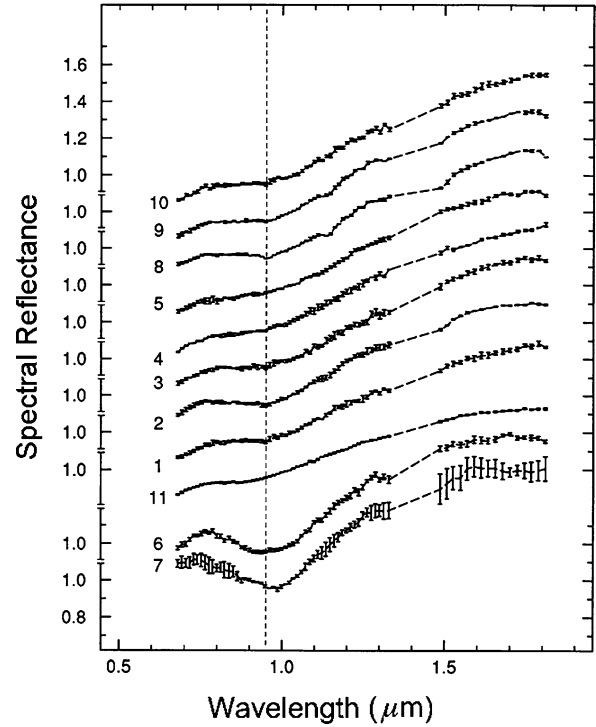

(a)

(b)

Fig. 10. (a) Near-IR reflectance spectra for the locations indicated in Fig. 9 and listed in Table 1. These spectra have been prepared for PCA by deleting the portions of the spectra susceptible to thermal contamination (longward of 2 μm) as well as the portions in the vicinity of telluric water absorptions (near 1.4 and 1.9 μm). The spectra have been offset for clarity and are scaled to 1.0 at 1.2 μm. The vertical dashed line is located at 0.95 μm. (b) Continuum-removed versions of the spectra shown in (a).

Spectral mixing model results (Table 2) suggest that highland material contributes 60% of the flux to the spectrum collected for the bright ray segment northeast of Seleucus
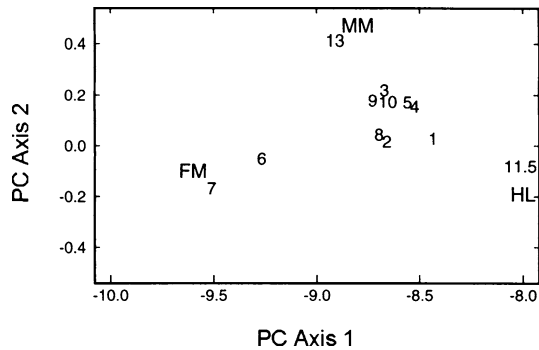

Fig. 11. Olbers A ray-related spectra projected into principal component space. The numbers identify spectra listed in Table 1 and shown in Fig. 10. Three plausible spectral endmembers were included in the PCA, and these plot near the extremes of a three-sided figure. The endmembers are indicated by MM (mature mare), FM (fresh mare), and HL (average highlands).

(no. 1). Immature mare debris is responsible for only 19% of the flux. The results for the diffuse ray segment (no. 9 and 10) indicate that lesser amounts of highland material are present.

The FeO and TiO_2 maps (Figs. 12b and 12c) also provide evidence for the presence of a significant nonmare component in the ray northeast of Seleucus. The ray exhibits FeO abundances of 13 to 16 wt% and TiO_2 values of 2 to 4 wt%. The adjacent mare basalt deposits have FeO values in excess of 16 wt% and TiO_2 values of 4 to 6 wt%. The ray is not distinct in the optical maturity image (Fig. 12d).

The evidence presented above indicates that significant amounts of highland material are present in the Olbers A ray segments near the ray intersection and northeast of Seleucus. The presence of this nonmare component is largely responsible for the high albedo of these ray segments. The presence of immature mare debris plays a subordinate role. We used the FeO, TiO_2, and optical maturity images (Fig. 12) to investigate the composition and origin of other portions of the Olbers A ray system shown in Fig. 12a. The ray segments
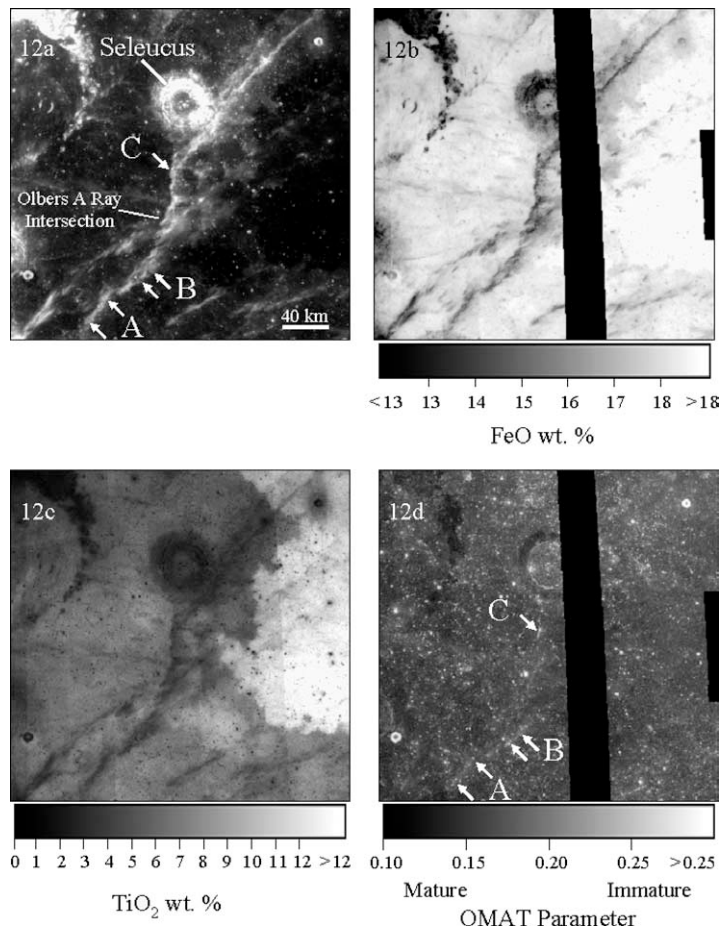

Fig. 12. (a) Clementine 750 nm image mosaic showing a portion of the Olbers A ray system in Oceanus Procellarum. The white arrows indicate three ray segments (A, B, and C) that are distinct in the optical maturity image. (b) FeO map derived from Clementine UVVIS images. The map is for the area shown in (a). (c) TiO_2 map derived from Clementine UVVIS images. The map is for the area shown in (a). (d) Optical maturity parameter image produced for a portion of the Olbers A ray system in Oceanus Procellarum. The arrows indicate three ray segments (A, B, and C) that are enriched in immature material relative to adjacent terrain. In these ray segments, immature material is associated with well-developed Olbers A secondary craters which excavated basaltic debris from beneath the regolith.

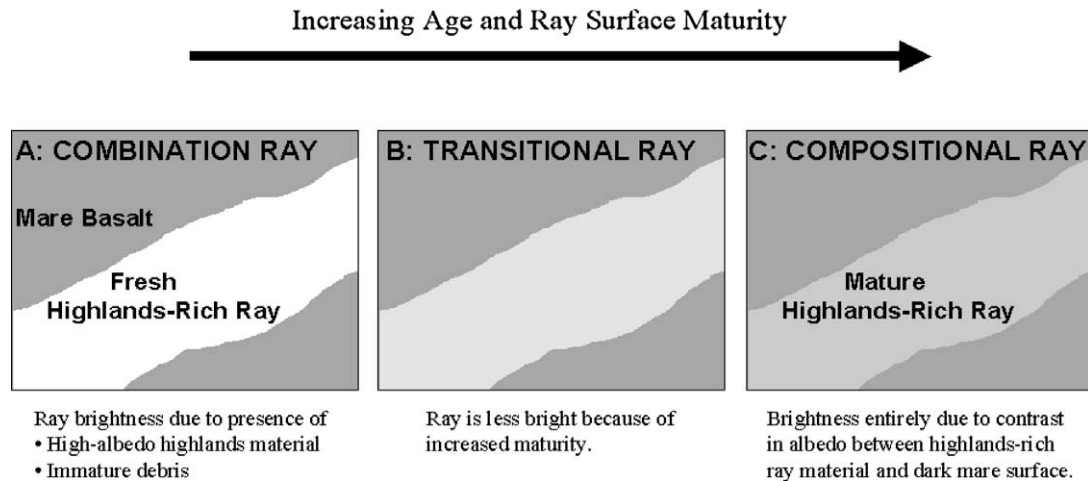Increasing Age and Ray Surface Maturity

Fig. 13. The evolution of a lunar combination ray. Panel A shows the ray immediately after it was formed by the emplacement of highlands ejecta on a dark mare surface. When first formed, combination rays contain immature highlands-rich primary ejecta and, in many instances, immature mare debris derived from secondary craters associated with the rays. The brightness of the ray is due to the presence of high-albedo highlands material and immature debris. Panel B shows a ray in transition. With increasing age, combination rays will become fainter as their surfaces mature. Panel C shows a fully mature compositional ray. Eventually, combination rays will evolve into compositional rays when their surfaces reach complete optical maturity. The brightness of a compositional ray is entirely due to the contrast in albedo between the highlands-rich ray material and the dark mare surface.

that appear bright in the 750 nm image also exhibit reduced FeO and TiO_2 values. This correlation indicates that non-mare material is present in the high-albedo ray segments. Most of these segments are not distinct in the optical maturity image (Fig. 12d). Hence, the presence of highland-rich primary ejecta from Olbers A is the dominant factor in producing the high albedo of these segments.

A small number of ray segments are distinct in the optical maturity image. They are enriched in immature material relative to adjacent terrain. Three of these segments are indicated by white arrows (A, B, and C) in Figs. 12a and 12d. In these three areas, the immature material is associated with well-developed Olbers A secondary craters which excavated basaltic debris from beneath the regolith. Support for this interpretation is provided by the radar data sets. Each of the three segments has slightly enhanced values in the depolarized 3.8-cm radar image, but no enhancement is apparent in the 70-cm data set. Hence, the upper portions of these ray segments are enriched in fragments in the 1–50 cm size range. Reduced FeO and TiO_2 values are also associated with these three segments. Therefore, both composition and immaturity are important in producing the brightness of these ray segments. These ray segments are good examples of "combination" rays.

3.6. Implications for the calibration of the lunar stratigraphic column

The results presented above as well as the findings of other investigations (Pieters et al., 1985; Campbell et al., 1992; Hawke et al. 1999, 2000; Grier and McEwen, 2001; Grier et al., 2001) have made it possible to understand the nature and origin of lunar crater rays. "Immaturity" rays exhibit high albedo values because of the presence of fresh

debris. For example, the rays associated with the Messier crater complex are composed of fresh mare material. The Tycho ray in the southern highlands exposes only immature nonmare material. These rays will become fainter with increasing age as the surfaces become more optically mature. The interiors of secondary craters will still be visible after the flat portions of ray become indistinct. Eventually, these rays will reach complete optical maturity and become indistinguishable from their surroundings.

Another class of rays exhibits high albedo values solely due to the differences in composition between the ray surfaces and nearby units. Mature "compositional" rays such as those associated with Lichtenberg crater are due entirely to the contrast in albedo between ray material containing highland-rich primary ejecta and the adjacent dark mare surfaces.

Both composition and immaturity play a role in producing a third class of lunar crater rays (Fig. 13). When first formed, these rays contain immature highland-rich primary crater ejecta and immature mare debris of local origin. With increasing age, these rays will become fainter as the surfaces mature. Eventually, these "combination" rays will evolve into compositional rays when their surfaces reach complete optical maturity.

It has long been thought that craters that exhibit rays were formed more recently than 1.1 Ga (e.g., Wilhelms, 1987). As discussed above, it has now been demonstrated that the rayed crater Lichtenberg is older than 1.68 Ga, perhaps far older (Hiesinger et al., 2003). Both Aristillus and Autolycus craters exhibit compositional rays that have reached complete optical maturity (Blewett and Hawke, 2001; Grier and McEwen, 2001; Grier et al., 2001). Ryder et al. (1991) proposed that Aristillus and Autolycus have absolute ages of 1.3 and 2.1 Ga, respectively, based on the results of radio-

metric dating of Apollo 15 samples. In addition, McEwen et al. (1993) used counts of craters superposed on large rayed-crater ejecta to determine that Hausen and Pythagoras have ∼ 3 Ga or greater ages. Since compositional rays can persist far longer than 1.1 Ga, it is not valid to assign a Copernican age to craters based only on the presence of rays.

Ryder et al. (1991) used the inferred age of Autolycus (2.1 Ga) to date the boundary of the Copernican and Eratosthenian Systems. At that time, the Eratosthenian–Copernican boundary date was thought to be about 1.1 Ga. This age was derived from an interpolation of the cratering-rate curve discussed by Wilhelms (1987). Ryder et al. (1991) noted that Autolycus was one of the most degraded rayed craters (Wilhelms, 1987) and assumed that Autolycus was one of the oldest Copernican craters. Under this assumption, they argued that it may be used to date the boundary of the Copernican with the Eratosthenian at a little over 2.1 Ga.

There are a number of problems with the analysis presented by Ryder et al. (1991). In order for their attempt to use the rayed ejecta of Autolycus to define and date the Copernican–Eratosthenian boundary to be valid, Autolycus would truly have to be the oldest Copernican-aged crater and its rays would have to be on the verge of disappearing. The compositional rays which surround Autolycus are optically mature and appear bright only because they contain relatively large amounts of highland debris (Blewett and Hawke, 2001; Grier et al., 2001; Grier and McEwen, 2001). This compositionally distinct ray material is an integral part of the regolith and the rays will be visible until this nonmare component has been thoroughly diluted with mare material by vertical impact mixing and lateral transport. Since this dilution process will require 100s of millions of years, the rays are not on the verge of disappearance (e.g., Pieters et al., 1985). In addition, Autolycus is clearly not the oldest rayed crater. As discussed above, several rayed craters have estimated ages of 3 Ga or more (e.g., McEwen et al., 1993). Autolycus appears very degraded because of the effects of the ejecta of the nearby crater Aristillus. We conclude that changing the age of the Copernican–Eratosthenian transition to 2.1 Ga is not justified.

The working distinction between the Eratosthenian and Copernican Systems is that Copernican craters larger than a few kilometers in diameter still have visible rays whereas Eratosthenian-aged craters do not (Shoemaker and Hackman, 1962; Wilhelms, 1987; Ryder et al., 1991). Since compositional rays can persist for 3 Ga or more, the mere presence of bright rays is not a reliable indicator that a crater was formed during the Copernican Period (e.g., McEwen et al., 1993, 1997; Hawke et al., 1996, 1999, 2000; Grier and McEwen, 2001; Pieters et al., 1985). It is clear that a new method is required to distinguish Copernican from Eratosthenian craters. Several workers (e.g., Hawke et al., 1999; Grier and McEwen, 2001; Grier et al., 2001) have suggested that the optical maturity parameter be used to define the Copernican–Eratosthenian boundary. The optical maturity

values for fresh crater ejecta decrease systematically with age (Lucey et al., 2000b). With increasing age, the optical maturity values from ejecta and rays becomes indistinguishable from the background values. This background value is the optical maturity index saturation point (Lucey et al., 2000b; Grier et al., 2001). The time required for a fresh surface to reach the optical maturity index saturation point could be defined as the Copernican Period. Surfaces that have reached full optical maturity would then be of Eratosthenian (or greater) age.

There are a number of problems associated with using OMAT values to define the Copernican–Eratosthenian boundary. Chief among these is that the amount of time required for a surface to reach full optical maturity has not been well established. In addition, the rate at which crater ejecta and rays change from immature to mature is controlled by several factors (e.g., Grier et al., 2001). These include the thickness of the ejecta deposit, the size of ejecta fragments, and the amount of mixing of primary ejecta with local, more-mature regolith material by secondary cratering during ejecta emplacement (e.g., Oberbeck, 1975). Differences in these factors could lead to variations in the amount of time required for various portions of a given ejecta deposit to reach full optical maturity. Grier et al. (2001) and Grier and McEwen (2001) presented radial profiles of OMAT values for large rayed craters and determined that for a fresh crater, the ejecta closest to the crater rim was the most immature and would appear so longer than more distal ejecta.

As described above, the time required for a surface to reach full optical maturity has not been firmly established. A possible solution to this problem has been proposed by Grier and co-workers (Grier et al., 2001; Grier and McEwen, 2001). They noted that if the ejecta of Copernicus crater were slightly more mature, it would be indistinguishable from the background in an OMAT image. The commonly accepted age of Copernicus is ∼ 0.8 Ga (Eberhardt et al., 1973; Bogard et al., 1994; Stöffler and Ryder, 2001). Hence, the saturation of the optical maturity index may occur at about 0.8 Ga.

4. Summary and conclusions

(1) Lunar crater rays are bright because of compositional contrast with the surrounding terrain, the presence of immature material, or some combination of the two.

(2) Mature "compositional" rays are due entirely to the contrast in albedo between ray material containing highland-rich primary ejecta and the adjacent dark mare surfaces. Compositional rays such as those associated with Lichtenberg crater do not disappear when the ray surfaces reach full optical maturity. These rays will become indistinct only when the highland material in the rays has been fully diluted by mare debris introduced by vertical mixing or lateral transport from adjacent mare units. It should be noted that

the mixing and dilution process takes much longer than the maturation process (e.g., Pieters et al., 1985).

(3) "Immaturity" rays are bright because of the presence of fresh, high-albedo material, which contrasts sharply with adjacent mature surfaces. This fresh, high-albedo material was produced as a result of one of the following mechanisms: (1) the emplacement of immature primary ejecta, (2) the deposition of immature local material ejected from secondary impact craters, (3) the action of debris surges moving downrange from secondary crater clusters, and (4) the presence of bright, immature interior walls of secondary impact craters. With increasing age, immaturity rays will become fainter as their surfaces approach optical maturity.

(4) Both composition and immaturity play a role in producing a third class of lunar crater rays. When first formed, these rays contain immature highland-rich primary crater ejecta and immature mare debris of local origin. With increasing age, these rays will become fainter as the surfaces mature. Eventually, these "combination" rays will evolve into compositional rays when their surfaces reach complete optical maturity.

(5) In the past, Lichtenberg has been mapped as a Copernican-aged crater. It has now been demonstrated that Lichtenberg is older than 1.68 Ga, perhaps much older (Hiesinger et al., 2003). Lichtenberg exhibits compositional rays. Other craters with compositional rays have also been shown to have ages significantly greater than 1.1 Ga (e.g., McEwen et al., 1993). Since compositional rays can persist far longer than 1.1 Ga, the mere presence of rays is not a reliable indicator of crater age. It is not valid to assign a Copernican age to craters based only on the presence of rays.

(6) A new method is required to distinguish Copernican from Eratosthenian craters. Several workers (e.g., Hawke et al., 1999; Grier et al., 2001) have suggested that the optical maturity parameter be used to define the Copernican–Eratosthenian boundary. The time required for a fresh surface to reach the optical maturity index saturation point could be defined as the Copernican Period. Surfaces that have reached full optical maturity would be of Eratosthenian (or greater) age.

(7) One problem with this suggestion is that the time required for a surface to reach full optical maturity has not been firmly established. In addition, the rate at which crater deposits mature is controlled by a number of factors (e.g., ejecta deposit thickness, size of ejecta fragments). Differences in these factors could lead to variations in the amount of time required for various portions of a given ejecta deposit to reach full optical maturity. A possible solution was suggested by the work of Grier and co-workers (Grier et al., 2001; Grier and McEwen, 2001). They noted that if the ejecta of Copernicus crater were slightly more mature, it would be indistinguishable from the optically mature background terrain. Since the commonly accepted age of Copernicus is ~ 0.8 Ga, the saturation of the optical maturity index may occur at about 0.8 Ga.

References

Adams, J.B., 1974. Visible and near-infrared diffuse reflectance spectra of pyroxenes as applied to remote sensing of solid bodies in the Solar System. J. Geophys. Res. 79, 4829–4836.

Allen, C.C., 1977. Rayed craters on the Moon and Mercury. Phys. Earth Planet. Inter. 15, 179–188.

Andre, C.G., Wolfe, R.W., Adler, I., 1979. Are early magnesium-rich basalts widespread on the Moon? In: Proc. Lunar Planet. Sci. Conf. 10th, pp. 1739–1751.

Baldwin, R.B., 1949. The Face of the Moon. Univ. of Chicago Press, Chicago.

Baldwin, R.B., 1963. The Measure of the Moon. Univ. of Chicago Press, Chicago.

Blewett, D.T., Hawke, B.R., 2001. Remote sensing and geologic studies of the Hadley–Apennine region of the Moon. Meteorit. Planet. Sci. 36, 701–730.

Blewett, D.T., Hawke, B.R., Lucey, P.G., Taylor, G.J., Jaumann, R., Spudis, P.D., 1995. Remote sensing and geologic studies of the Schiller–Schickard region of the Moon. J. Geophys. Res. 100, 16959–16977.

Blewett, D.T., Lucey, P.G., Hawke, B.R., Jolliff, B.L., 1997. Clementine images of the sample-return stations: refinement of FeO and TiO_2 mapping techniques. J. Geophys. Res. 102, 16319–16325.

Bogard, D.D., Garrison, D.H., Shih, C.-Y., Nyquist, L.E., 1994. ^{40}Ar–^{39}Ar dating of two lunar granites: the age of Copernicus. Geochim. Cosmochim. Acta 58, 3093–3100.

Campbell, B.A., Bell III, J.F., Zisk, S.H., Hawke, B.R., Horton, K.A., 1992. A high-resolution and CCD imaging study of crater rays in Mare Serenitatis and Mare Nectaris. In: Proc. Lunar Planet. Sci. Conf. 22nd, pp. 259–274.

De Hon, R.A., 1979. Thickness of the western mare basalts. In: Proc. Lunar Planet. Sci. Conf. 10th, pp. 2935–2955.

Eberhardt, P., Geiss, J., Grögler, N., Stettler, A., 1973. How old is the crater Copernicus? Moon 8, 104–114.

Green, J., 1971. Copernicus as a lunar caldera. J. Geophys. Res. 76, 5719–5731.

Grier, J.A., McEwen, A.S., 2001. The lunar record of recent impact cratering. In: Peuckner-Ehrenbrink, B., Schmitz, B. (Eds.), Accretion of Extraterrestrial Matter throughout Earth History. Kluwer Academic, Norwell, MA, pp. 403–422.

Grier, J.A., McEwen, A.S., Lucey, P.G., Milazzo, M., Strom, R.G., 2001. Optical maturity of ejects from large rayed lunar craters. J. Geophys. Res. 106, 32847–32862.

Hawke, B.R., Blewett, D.T., Bell III, J.F., Lucey, P.G., Campbell, B.A., Robinson, M.S., 1996. Remote sensing studies of lunar crater rays. In: Lunar Planet. Sci. XXVII, pp. 507–508.

Hawke, B.R., Blewett, D.T., Lucey, P.G., Peterson, C.A., Bell III, J.F., Campbell, B.A., Robinson, M.S., 1999. The composition and origin of selected lunar crater rays. In: New Views of the Moon II: Understanding the Moon through the Integration of Diverse Datasets. Lunar and Planetary Institute, Houston, TX, pp. 22–23.

Hawke, B.R., Blewett, D.T., Lucey, P.G., Peterson, C.A., Bell III, J.F., Campbell, B.A., Robinson, M.S., 2000. Lunar crater rays: compositions

and modes of origin. In: Lunar Planet. Sci. XXXI. Abstract 1333 [CD-ROM].

Hiesinger, H., Head III, J.W., Wolf, U., Jaumann, R., Neukum, G., 2003. Ages and stratigraphy of mare basalts in Oceanus Procellarum, Mare Nubium, Mare Cognitum, and Mare Insularum. J. Geophys. Res. 108 (E7), 5065. doi:10.1029/2002JEOO1985.

Johnson, P.E., Smith, M.O., Adams, J.B., 1985. Quantitative analysis of planetary reflectance spectra with principal components analysis. In: Proc. Lunar Planet. Sci. Conf. 15th, pp. C805–C810.

Lucchitta, B.K., 1977. Crater cluster and light mantle at the Apollo 17 site: a result of secondary impact from Tycho. Icarus 30, 80–96.

Lucey, P.G., Hawke, B.R., Pieters, C.M., Head, J.W., McCord, T.B., 1986. A compositional study of the Aristarchus region of the Moon using near-infrared reflectance spectroscopy. In: Proc. Lunar Planet. Sci. Conf. 16th, pp. D344–D354.

Lucey, P.G., Taylor, G.J., Malaret, E., 1995. Abundance and distribution of iron on the Moon. Science 268, 1150–1153.

Lucey, P.G., Blewett, D.T., Hawke, B.R., 1998. Mapping FeO and TiO_2 content of the lunar surface with multispectral imagery. J. Geophys. Res. 103, 3679–3699.

Lucey, P.G., Blewett, D.T., Jolliff, B.L., 2000a. Lunar iron and titanium abundance algorithms based on final processing of Clementine UV-VIS data. J. Geophys. Res. 105, 20297–20305.

Lucey, P.G., Blewett, D.T., Taylor, G.J., Hawke, B.R., 2000b. Imaging of lunar surface maturity. J. Geophys. Res. 105, 20377–20386.

Mackin, R.J., 1968. Current Knowledge of the Moon and Planets. Mobil Research and Development Corporation, Dallas, TX.

McCord, T.B., Clark, R.N., Hawke, B.R., McFadden, L.A., Owensby, P.D., Pieters, C.M., Adams, J.B., 1981. Moon: near-infrared spectral reflectance, a first good look. J. Geophys. Res. 86, 10883–10892.

McEwen, A.S., Gaddis, L.R., Neukum, G., Hoffman, H., Pieters, C.M., Head, J.W., 1993. Galileo observations of post-Imbrium craters during the first Earth–Moon flyby. J. Geophys. Res. 98, 17207–17231.

McEwen, A.S., Moore, J.M., Shoemaker, E.M., 1997. The Phanerozoic impact cratering rate: evidence from the farside of the Moon. J. Geophys. Res. 102, 9231–9242.

Moore, H.J., 1967. Geological map of the Seleucus quadrangle of the Moon. USGS Map I-527.

Morrison, R.H., Oberbeck, V.R., 1975. Geomorphology of crater and basin deposits: emplacement of the Fra Mauro formation. In: Proc. Lunar Planet. Sci. Conf. 6th, pp. 2503–2530.

Nasmyth, J., Carpenter, J., 1885. The Moon. Scribner and Welford, New York.

Oberbeck, V.R., 1971. A mechanism for the production of lunar crater rays. Moon 2, 263–278.

Oberbeck, V.R., 1975. The role of ballistic erosion and sedimentation in lunar stratigraphy. Rev. Geophys. Space Phys. 13, 337–362.

Oberbeck, V.R., Hörz, F., Morrisson, R.H., Quaide, W.L., Gault, D.E., 1975. On the origin of the lunar smooth-plains. Moon 12, 19–54.

Pieters, C.M., Adams, J.B., Mouginis-Mark, P.J., Zisk, S.H., Smith, M.O., Head, J.W., McCord, T.B., 1985. The nature of crater rays: the Copernicus example. J. Geophys. Res. 90, 12393–12413.

Ryder, G., Bogard, D., Garrison, D., 1991. Probable age of Autolycus and calibration of lunar stratigraphy. Geology 19, 143–146.

Schmitt, H.H., Trask, N.J., Shoemaker, E.M., 1967. Geological map of the Copernicus quadrangle of the Moon. USGS Map I-515.

Schultz, P.H., 1976. Moon Morphology. Univ. of Texas Press, Austin.

Schultz, P.H., Gault, D.E., 1985. Clustered impacts: experiments and implications. J. Geophys. Res. 90, 3701–3732.

Schultz, P.H., Spudis, P.D., 1983. The beginning and end of lunar mare volcanism. Nature 203, 233–236.

Shoemaker, E.M., 1962. Interpretation of lunar craters. In: Kopal, Z. (Ed.), Physics and Astronomy of the Moon. Academic Press, New York, pp. 283–359.

Shoemaker, E.M., 1966. Preliminary analysis of the fine structure of the lunar surface in Mare Cognitum. In: Hess, W.N., Menzel, D.H., O'Keefe, J.A. (Eds.), The Nature of the Lunar Surface. Johns Hopkins Press, Baltimore, pp. 23–77.

Shoemaker, E.M., Hackman, R.J., 1962. Stratigraphic basis for a lunar time scale. In: Kopal, Z., Mikhailov, Z.K. (Eds.), The Moon—Symposium 14 of the Internation Astronomical Union. Academic Press, New York, pp. 289–300.

Shoemaker, E.M., Batson, R.M., Holt, H.E., Morris, E.C., Rennilson, J.J., Whitaker, E.A., 1969. Observations of the lunar regolith and the Earth from the television camera on Surveyor 7. J. Geophys. Res. 74, 6081–6119.

Smith, M.O., Johnson, P.E., Adams, J.B., 1985. Quantitative determination of mineral types and abundances from reflectance spectra using principal components analysis. In: Proc. Lunar Planet. Sci. Conf. 15th, pp. C797–C804.

Stöffler, D., Ryder, G., 2001. Stratigraphy and isotope ages of lunar geologic units: chronological standard for the inner Solar System. Space Sci. Rev. 96, 9–54.

Thompson, T.W., 1987. High-resolution lunar radar map at 70-cm wavelength. Earth Moon Planets 37, 59–70.

Tomkins, H.G., 1908. Note on the bright rays on the Moon. B.A.A. 18, 126.

Trask, N.J., Rowan, L.C., 1967. Lunar orbiter photographs: some fundamental observations. Science 158, 1529–1535.

Whitaker, E.A., 1966. The surface of the Moon. In: Hess, W.N., Menzel, D.H., O'Keefe, J.A. (Eds.), The Nature of the Lunar Surface. Johns Hopkins Press, Baltimore, pp. 79–98.

Whitaker, E.A., Kuiper, G.P., Hartmann, W.K., Spradley, L.H., 1963. Rectified lunar atlas, supplement number two to the USAF lunar atlas. U.S. Air Force Aeronautical Chart and Information Center, St. Louis, MO.

Wilhelms, D.E., 1987. The Geologic History of the Moon. USGS Prof. Paper 1348.

Zisk, S.H., Pettengill, G.H., Catuna, G.W., 1974. High-resolution radar map of the lunar surface at 3.8-cm wavelength. Moon 10, 17–50.